Stapp Car Crash Journal 44 (November 2000) 315-334

Car Crash Journal

2000-01-SC21

Development and Validation of a Pedestrian Lower Limb Non-Linear 3-D Finite Element Model

Peter J. Schuster, Clifford C. Chou, Priya Prasad
Ford Motor Company

Gopal Jayaraman
Michigan Technological University

ABSTRACT

Lower limb injury is becoming an increasingly important concern in vehicle safety for both occupants and pedestrians. To enable vehicle manufacturers to better understand the biomechanical effects of design changes, it is deemed beneficial to employ a biomechanically fidelic finite element model of the human lower limb.

The model developed in this study includes long bones (tibia, fibula, femur) and flat bone (patella) as deformable bodies. The pelvis and foot bones are modeled as rigid bodies connected to the femur and tibia/fibula via rotational spring-dashpots. The knee is defined by scanned bone surface geometry and is surrounded by the menisci, major ligaments, and patellar tendon. Finite elements used to model include 6- and 8-node solids for cartilage, menisci, surrounding muscles, and cancellous bone; 3- and 4-node shells for skin and cortical bone; and nonlinear spring-dashpots for ligaments. Anatomical, physiological, and material properties data are from the literature while the bone surface geometry was scanned by a commercial source.

Validation against published cadaver test results consisted of tibia and femur 3-point bending (lateral-medial and anterior-posterior) and whole limb lateral knee shear. Validation was performed under both static and dynamic loading conditions, until bone failure or ligament rupture. Additional dynamic validation with the lower limb in a seated orientation has not been completed, limiting current applications to the pedestrian impact condition. The validated models were employed to examine the effect of axial compressive force (the physiological condition) on tibia and femur lateral-medial and anterior-posterior bending under static conditions.

INTRODUCTION

Extensive research and development by auto manufacturers and legislators over the past three decades has resulted in significant improvements in vehicle safety. An example of the benefits of this work is that automotive-related fatalities decreased by 12% between 1988 and 1998 in the U.S. However, in the same time period, automotive injuries dropped only 6.5% [1]*. An awareness of this trend has resulted in increased efforts to reduce the accident injury risk to automotive occupants and pedestrians.

In vehicle frontal accidents, lower limb trauma comprises 16-25% of all AIS 2+ occupant injuries [2]. The most common injuries are fractures, dislocations, and ligamentous damage [3,4]. In pedestrian accidents, lower limb trauma constitute 30-40% of all injuries [5,6], with tibia or femur shaft fracture and knee joint damage (including intra-articular fractures and ligament rupture or avulsion) being the most common injuries [7]. While not typically life-threatening, lower limb injuries can require long recovery times or result in permanent disability.

To predict the risk of pedestrian or occupant lower limb injury in an impact, physical test devices are typically used. These devices are designed to predict specific injury modes under certain impact conditions in an objective, repeatable manner. The most commonly used devices for predicting lower limb injury in the automotive environment are the Hybrid III Dummy lower limb and the EEVC† Pedestrian Leg-Form. The Hybrid III Dummy lower limb is designed to predict tibia or femur fracture (based on forces and bending moments) when used in a seated position and impacted from the front. The EEVC Pedestrian Leg-Form predicts tibia fracture or knee joint

* Numbers in brackets designate references at the end of the paper.

† EEVC – European Enhanced Vehicle-safety Committee

injury (based on acceleration, bending angle, and shear displacement) when used in a standing position and impacted from the side.

While the development and use of these physical test devices is essential for final production verification purposes, they have inherent limitations, including:

- They are only functionally representative of a human lower limb for one set of impact conditions.
- They do not respond like a human lower limb since the materials and geometry are not the same.
- They can only measure forces, moments, and displacements at specific locations, rather than the local stress and strain that actually determine when and where injuries occur.
- The established criteria relating the measured quantities to the occurrence of certain injuries are only valid in a limited range of impact conditions.
- As they cannot change stiffness or shape after an injury is predicted, they cannot determine the interaction between different types of injuries.
- They simulate a single set of boundary conditions.

Finite Element (FE) models, once developed and validated, can provide a better prediction of injuries using a variety of impact conditions, boundary conditions, and material properties. An FE model can predict the local stress and strain and directly determine failure using the accepted material failure criteria. It can be accurate in its anatomical and material properties and even change its stiffness or configuration when an injury occurs. Due to these capabilities, FE models can be used to develop failure criteria under combined loading conditions to better enable physical test devices to predict injuries. The main limitations of FE models are that their accuracy is dependent on the input material properties and modeling quality and they can only be used to evaluate mathematical simulations of vehicles, not physical parts.

The paper begins with a review of the benefits and limitations of existing lower limb finite element models. To overcome some of the limitations, an improved FE model—more closely representing the human lower limb—was developed. Following a description of this improved model, the static and dynamic validation is presented. The paper concludes with a first application of the model – an examination of the influence of axial load on the bending performance of the lower limb long bones.

The detailed lower limb finite element model was developed in this study for the evaluation of automotive accident injury risk. Since the first application will be for pedestrian lower limb injuries (which are primarily in the tibia, femur, and knee joint), the improved model does not include a detailed foot, hip joint, or ankle joint. A detailed foot and ankle model being developed in a separate study will be merged with this lower limb model in the future for occupant injury assessment. The model does not currently predict the kinematics, dynamics, deformation, or injuries beyond the lower limb, but it is capable of being combined with other body segment models to create a full human 3-D FE model at a later date.

BACKGROUND

EXISTING LOWER LIMB FE MODELS – Lower limb finite element models can be categorized as one of four types, listed by increasing complexity:

1. Rigid bones with defined joints.
2. Deformable bones with defined joints.
3. Rigid bones with interfacing soft tissues and connecting ligaments.
4. Deformable bones with interfacing soft tissues and connecting ligaments.

Over the past six years several lower limb FE models falling roughly into one of these four types have been developed. For the most part, these models have been designed to perform well in one particular situation—such as seated frontal impact or standing lateral impact—rather than under several different impact conditions.

Rigid Bones with Defined Joints – Since using defined joints effectively removes the complex joint contact surfaces from the analysis, the modeling task can be greatly simplified. However, this choice means that the model cannot directly predict intra-articular injuries – the most debilitating lower limb injury. Also, modeling the bones as rigid bodies simplifies the modeling since rigid body element quality does not affect prediction accuracy and the geometry does not affect rigid body strength. The trade-offs are that bone failure strength cannot be predicted and the bone stiffness will be considered infinite. These models need joint properties as input and rely on derived injury criteria. However, computation time for this type of FE model is a minimum.

In 1998, Bedewi [8] and Wykowski, *et al.* [3] independently developed lower limb models for occupant frontal impact analysis in DYNA3D and PAM-CRASH, respectively. In both models, the sub-talar, ankle, knee, and hip were included as defined joints while all lower limb bones were represented by rigid bodies. Bone geometry came from Viewpoint Datalabs.

Deformable Bones with Defined Joints – This type of model is more complex to develop since bone geometry and element quality become important for accuracy. However, since the joint surfaces are not critical for contacts, some modeling and computation time is saved. By including deformable bones, bone failure can be predicted, but intra-articular damage prediction still

depends on derived criteria. This type of model also needs joint properties as input.

While none of the recent FE models have followed this type overall, two have used simplified knee joint geometry to reduce modeling complexity. In 1994, Bermond, *et al.* [9] developed a model including the tibia, femur, ACL[4], LCL[5], MCL[6], and PCL[7] for pedestrian impact analysis using PAM-CRASH. The bones were modeled as deformable bodies using linear viscoelastic shell elements: 650 for the femur and 550 for the tibia. Ligaments were modeled as 1-D non-linear linkage elements. Bone geometry came from scanned bone surfaces.

In 1996, Yang, *et al.* [10] developed a model including the tibia, femur, ACL, LCL, MCL, PCL, and simplified foot for pedestrian impact analysis using DYNA3D. The bones were modeled as deformable bodies using linear viscoelastic solid hexahedron elements: 3072 for the femur and 5364 for the tibia. Collateral ligaments were modeled with a combination of shell and spring elements while cruciate ligaments were modeled with spring-damper elements. Bone geometry was simplified to reduce the modeling complexity and smooth the contact surfaces.

Rigid Bones with Interfacing Soft Tissues and Connecting Ligaments – By including soft tissues and ligaments at the knee joint, a model can more accurately predict motion of the knee under various conditions along with soft tissue injuries. However, since the bones are modeled as rigid bodies, neither bone failure nor the interactions between bone failure and ligament injury can be predicted.

Between 1995 and 1998, Bendjaballah, *et al.* [11] developed a model including the distal femur, proximal tibia, patella, cartilage, menisci, ACL, LCL, MCL, and PCL for various knee joint studies under different loading directions using an in-house finite element package. The bones and cartilage were modeled as rigid bodies and 8-node solid elements, respectively. The menisci were modeled using 8-node solid elements with reinforcing truss elements. Ligaments consisted of uniaxial elements. Bone geometry was based on CT-scans of human bones.

In 1999, Li, *et al.* [12] developed a model of the distal femur, proximal tibia, cartilage, menisci, ACL, LCL, MCL, and PCL for various knee joint studies using ABAQUS. The bones and cartilage were modeled as rigid bodies and 8-node linear-elastic solid elements, respectively. Ligaments and menisci were included as non-linear elastic springs. The geometry was obtained from magnetic resonance images of a cadaveric knee specimen.

Deformable Bones with Interfacing Soft Tissues and Connecting Ligaments – This type of model can directly predict both ligament/soft tissue and bone failure injuries, allowing the interdependency of bone/ligament/soft tissue injury to be studied. As a result, however, it requires the most modeling effort and computational time. The recent model developed by Iwamoto, *et al.* [13] included all lower limb bones, major ligaments and tendons, and patellar cartilage for occupant frontal impact analysis using PAM-CRASH. Cortical and cancellous bone were modeled as deformable shell and solid elements, respectively. Ligaments were modeled with elastic membrane (tension-only) elements while tendons used bar elements. Bone geometry came from Viewpoint Datalabs.

Table 1 summarizes the relative benefits and limitations of the four modeling types discussed above. Table 2 lists the recently published lower limb finite element models, summarizing the relevant characteristics of each model along with the modeling type.

AREAS FOR IMPROVEMENT – Following the review of current models, three areas were identified where an improved model would be beneficial. These are:

- Bone and Soft Tissue Modeling
- Injury Prediction & Interactions
- Stress/Strain Based Injury Criteria

Bone and Soft Tissue Modeling – Complete modeling of the fibula, patella, menisci, and cartilage as dimensionally correct deformable bodies with appropriate material properties and failure criteria. Only one of the existing models contains the fibula and patella as deformable bodies. Deformable models of the fibula and patella allow these bone injuries to be captured and can improve the model's prediction of lower limb strength. Only three of the models include the cartilage and menisci and none include the surrounding muscles. Contact stresses cannot be accurately predicted without the cartilage, menisci, and surrounding muscles modeled. Existing models either do not include cancellous bone or include it throughout the long bones. The stress prediction in the cortical bone becomes less accurate with either assumption.

Injury Prediction & Interdependency – Prediction of the common lower limb injuries and how they interact during an impact. While two of the existing models can predict bone failure and ligament rupture injuries, it is unclear whether they can also model the effects of these injuries on subsequent deformation. Modeling these effects is important since a bone failure or ligament rupture can significantly reduce the stress in other areas of the lower limb. A model that does not change bone or ligament

[4] ACL = Anterior Cruciate Ligament
[5] LCL = Lateral Collateral Ligament
[6] MCL = Medial Collateral Ligament
[7] PCL = Posterior Cruciate Ligament

Table 1: Scope and Limitations of Lower Limb Finite Element Modeling Types

	Modeling Type	*Scope*	*Limitations*
1	**Rigid bones with defined joints**	Minimum computation time for a finite element model.	Need joint properties as input. Only derived injury criteria can be used.
2	**Deformable bones with defined joints**	Bone failure can be predicted.	Need joint properties as input. Ligament injury cannot be predicted.
3	**Rigid bones with interfacing soft tissues and connecting ligaments**	Ligament and soft tissue injuries can be predicted.	Bone failure cannot be predicted. Cannot determine interdependencies between failure mechanisms.
4	**Deformable bones with interfacing soft tissues and connecting ligaments**	Bone failure and ligament/soft tissue injuries can be predicted. Interdependencies of these failure mechanisms can be modeled.	Maximum computation time required.

Table 2: Characteristics of Current Knee Joint / Lower Limb Finite Element Models

Source	*Type*	*Bones Modeled*					*Soft Tissues Modeled*				*Injury Prediction*		
		Femur	*Tibia*	*Fibula*	*Patella*	*Cancellous Bone*	*Cartilage*	*Major Ligaments**	*Menisci*	*Surrounding Muscles*	*Bone Failure*	*Ligament Rupture*	*Menisci Tear*
Bedewi [8]	1	R	R	R	R	N	N	N	N	N	N	N	N
Bendjaballah, *et al.* [11]	3	R†	R†	N	R	N	D	D	D	N	N	N	N
Bermond, *et al.* [9]	2/4	D	D	N	N	N	N	D	N	N	Y	Y	N
Iwamoto, *et al.* [13]	4	D	D	D	D	D	D	D	N	N	Y	N	N
Li, *et al* [12]	3	R†	R†	N	R	N	D	D	D	N	N	N	N
Wykowski, *et al.* [3]	2	R	R	R	R	D	N	D	D	N	N	N	N
Yang, *et al.* [10]	2/4	D‡	D‡	N	N	D	N	D	N	N	Y	Y	N
Present Study	4	D	D	D	D	D	D	D	D	D	Y	Y	Y

R = modeled as a rigid body
D = modeled as a deformable body
N = not included in model
Y = both injury and effect of injury on further deformation is predicted

* Major ligaments include the ACL, LCL, MCL, PCL, and patellar and quadriceps tendons.
† Only part of the bone included, close to the knee joint.
‡ Simplified bone geometry. No cortical bone modeled.

stiffness after injury risks predicting further injuries that a human would not receive. In addition to these concerns, no existing model predicts the meniscus or cartilage injuries that can result in long-term functional loss, such as with degenerative arthritis.

Stress/Strain Based Injury Criteria – Establish new injury criteria for physical test devices based on the prediction of injuries with the model. The number of tests that can be performed with cadaveric specimens is necessarily limited by the testing cost and availability of appropriate samples. A validated FE model that predicts injuries based on the local stress and strain can be used to determine derived injury criteria under a variety of impact conditions. Current or modified physical test devices can then rely on these derived criteria to better predict injuries under different conditions.

To implement these enhancements, the development of an improved lower limb finite element model using minimum assumptions was undertaken. This improved model can predict not only the occurrence of bone failure, ligament rupture, and meniscus tear, but also how each of these injuries will influence the subsequent deformation of the lower limb. It can be used to examine and improve the existing derived injury criteria.

MODEL DEVELOPMENT

Since the purpose of this model is to enable evaluation of the real-world performance of vehicle designs in lower limb injury, it was important to use a compatible finite element solver. As Radioss is the primary non-linear FE code used at Ford Motor Company for vehicle program and crash analysis, this model was developed using Radioss© [1] version 4.1 to allow it to be readily used for vehicle crash simulation and program implementation. The model was constructed using two main pre-processors: ICEM CFD HEXA© [2] was used to create the cancellous bone finite elements, while Hypermesh© [3] version 3.1 was used for the rest of the finite elements.

GEOMETRY – The lower limb bones form the basis for the model geometry. The sources for the lower limb geometry data are listed in Table 3. The femur, tibia, fibula, and patella IGES [4] surfaces created by Viewpoint Datalabs were obtained from Bedewi [8]. Cortical bone thickness was set based on bone dimensions reported by Cristofolini, *et al.* [14,15]. The volume occupied by cancellous bone in the long bones was determined by comparison with images from the Visible Human Project© [16]. The correct bone position and orientation in full extension were determined from figures in Warwick & Williams [17] and the Visible Human Project [16]. The foot and calcaneus models were taken from the Ford Motor Company Hybrid III Dummy FE model. The ankle, subtalar, and hip joint properties were obtained from P. Bedewi [8].

The soft tissue descriptions were also obtained from several sources. IGES surfaces defining the skin were developed in Ramsis© [5] version 3.4.1 for a 50th percentile German adult male. Ligament insertion locations and slack lengths were obtained from Yang & Kajzer [18] and Moeinzadeh & Engin [19]. The size and shape of the attachment areas were derived from the figures in Girgis, *et al.* [20] and Warwick & Williams [17]. The thickness of cartilage elements above the bone surfaces were determined from cartilage thickness maps given in Mow & Hayes [21] and Mow, *et al.* [22]. The menisci geometries were determined from top view diagrams in Mow, *et al.* [23], cross-section diagrams in Mow, *et al.* [22], and the distance between the tibia and femur cartilage surfaces.

The finite element model was constructed using the established Ford Motor Company best practices for model quality, including element size, % degenerate elements, warpage, aspect ratio, skew, and jacobian. ICEM CFD HEXA was used to structure a hexahedral mesh inside the bone IGES surfaces. Shell finite elements with thickness ranging from 2.0 mm (for proximal/distal femur & tibia, fibula, and patella) to 5.0 mm (for femur mid-shaft) were created on the surface of this mesh to model the cortical bone. The cancellous bone was modeled with solid hexahedral finite elements throughout the fibula and patella and in the distal and proximal ends of the femur and tibia. No cancellous bone was included in the central two-thirds of the femur and tibia.

Cartilage finite elements were created based off the bone finite elements. A single layer of solid 6- and 8-node finite elements was modeled on the tibial plateau, femur condyles, and patella to represent the cartilage. The menisci were included as a double layer of solid 6- and 8-node finite elements offset 1.0 mm between the femur condyle and tibial plateau cortical bone surfaces. Each ligament was modeled as several one-dimensional nonlinear spring-dashpot finite elements connected in series between the attachment points. Hypermesh was used to create the skin shell and surrounding muscle solid finite elements from the IGES surfaces. The surrounding muscle solid elements that interfered with the bone model were then removed to allow contacts between the muscle and bone.

Contacts between the bone, surrounding muscles, cartilage, menisci, and ligaments were modeled using a Slide/Void Multipurpose Interface (Type 7) with a 1.0 mm gap. The connection between the ligament attachment nodes and the bone shell elements in the insertion area were modeled with a Tied Connection Interface (Type 2). Hip, ankle (flexion-extension), and sub-talar (inversion-eversion) joints were created with non-linear rotational spring-dashpot finite elements (Type 8 general springs with translation along all three directions constrained) connecting the pelvis and foot rigid bodies to the proximal femur and distal tibia. Rigid bodies were created encompassing 40 mm at the proximal end of the femur and 35 mm at the distal end of the tibia and fibula to attach to these spring-dashpot finite elements. By preventing translation within the joints and attaching to rigid bodies, the most adverse conditions related to lower limb injury are simulated. Spring properties were based on the physiological joint stiffness.

Figure 1 and Figure 2 provide illustrations of the lower limb finite element mesh, while Table 4 summarizes the modeling techniques.

MATERIAL PROPERTIES – Where available, the material properties used in the model represent the median of the published data. Those parameters not found in the literature were set based on simple analyses, as described below. Since material models for biological materials do not exist in Radioss and the

[1] Radioss is an explicit 3-D non-linear dynamic finite element program developed by Mecalog, France.
[2] ICEM CFD Hexa is a product of ICEM CFD Engineering, USA.
[3] Hypermesh is a product of Altair Enineering, USA.
[4] IGES = Initial Graphics Exchange Specification, a file format for exchanging graphics data.
[5] RAMSIS is a product of TecMath GmbH, Germany.

Table 3: Sources of Lower Limb Geometry Data

Geometry	*Source*
Cortical Bone Surface	Bedewi [8] (Viewpoint Datalabs)
Cortical Bone Thickness	Cristofolini, *et al.* [14,15]
Cancellous Bone	Visible Human Project© [16]
Skin Surfaces	Ramsis© version 3.4.1
Ligament Insertion Locations	ACL, LCL, PCL: Yang & Kajzer [18] MCL: Moeinzadeh & Engin [19]
Ligament Insertion Size	Girgis, *et al.* [20], Warwick & Williams [17]
Cartilage	Mow & Hayes [21], Mow, *et al.* [22]
Menisci	Mow, *et al.* [22,23]
Foot	Ford Motor Company Hybrid III model
Hip, Ankle, Sub-Talar Joints	Bedewi [8], passive properties
Bone Orientation	Warwick & Williams [17], Visible Human Project© [16]

Table 4: Component Finite Element Modeling Techniques

Component	*Modeling Technique*
Tibia, Femur	Cortical bone: 3- and 4-node shell elements on surface, 2.0 mm (ends) to 5.0 mm (mid-shaft) thick. Cancellous bone: 6- and 8-node solid elements at proximal & distal ends. Shared node connections.
Fibula, Patella	Cortical bone: 3- and 4-node shell elements on surface, 2.0 mm thick. Cancellous bone: 6- and 8-node solid elements throughout volume. Shared node connections.
Cartilage	Single layer of 6- and 8-node solid elements. Shared node connections with underlying cortical bone.
Menisci	Double layer of 6- and 8-node solid elements. Simple springs connect to tibial plateau and LCL.
Ligaments	Single row of spring-dashpot elements connected in series. Kinematic constraints to cortical bone shell elements at insertions.
Skin, Surrounding Muscles	Skin: 4-node shell elements at surface. Surrounding Muscles: 8-node solid elements throughout volume. Shared node connections
Hip, Ankle Joints	Rigid bodies comprised of proximal 10% of femur and distal 10% of tibia & fibula connected by rotational spring-dashpot elements to the pelvis and calcaneus rigid bodies.
Foot, Sub-talar Joint	Entire foot as rigid body. Connected by rotational spring-dashpot elements to the calcaneus rigid body.

creation of a new material model is beyond the scope of this study, the most appropriate material models from those currently available were used. The selected material models and property sources are identified in Table 5.

Cortical and Cancellous Bone – Bone is an orthotropic material that can be approximated as transversely isotropic (TI) with distinct non-linear compressive and tensile properties. Material Type 25 (Composite Shell) and Material Type 14 (Composite [Solid] Material) are capable of modeling these characteristics with the same elastic modulus in tension and compression.

Element failure (deletion) in these material types is determined using a distortion energy failure criterion. In a recent study evaluating various failure theories for bone, Keyak & Rossi [24] found that "the distortion energy and τ_{max} failure theories were the most robust of those examined, providing the most consistently strong FE model performance for two very different loading conditions."

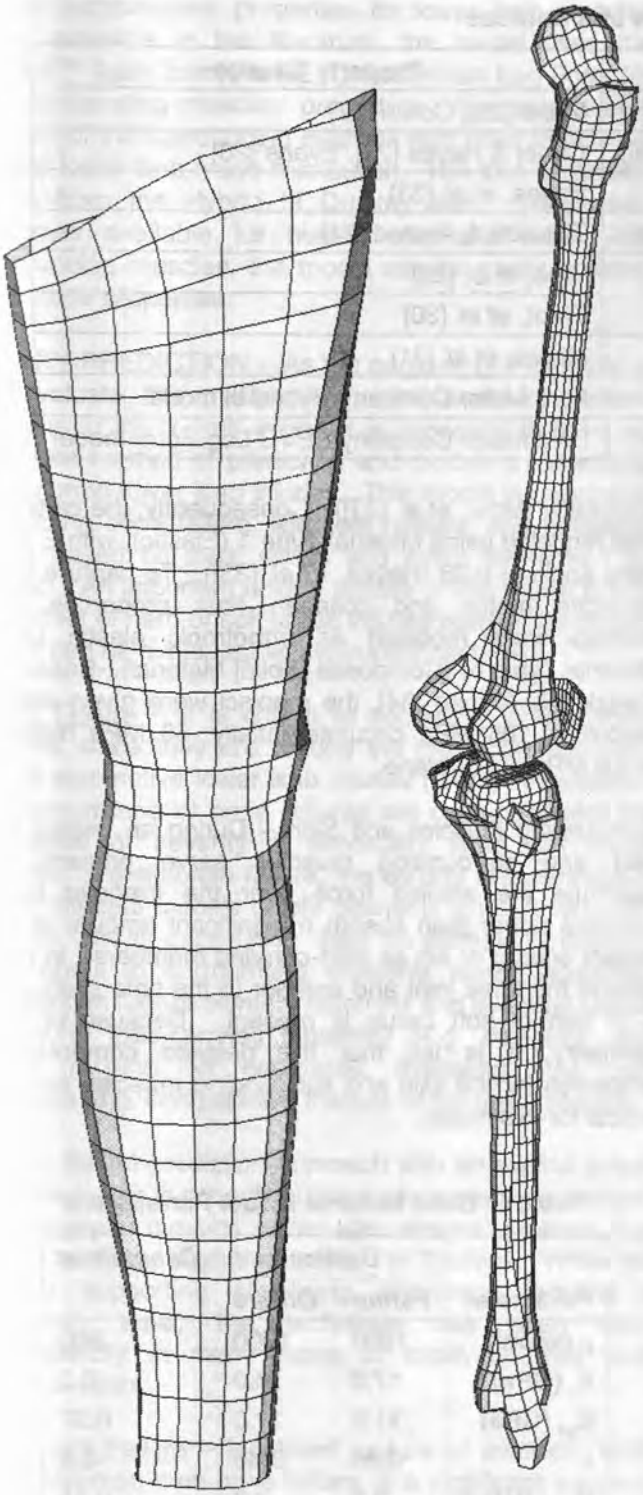

Figure 1: Lower Limb Skin & Bone Finite Elements

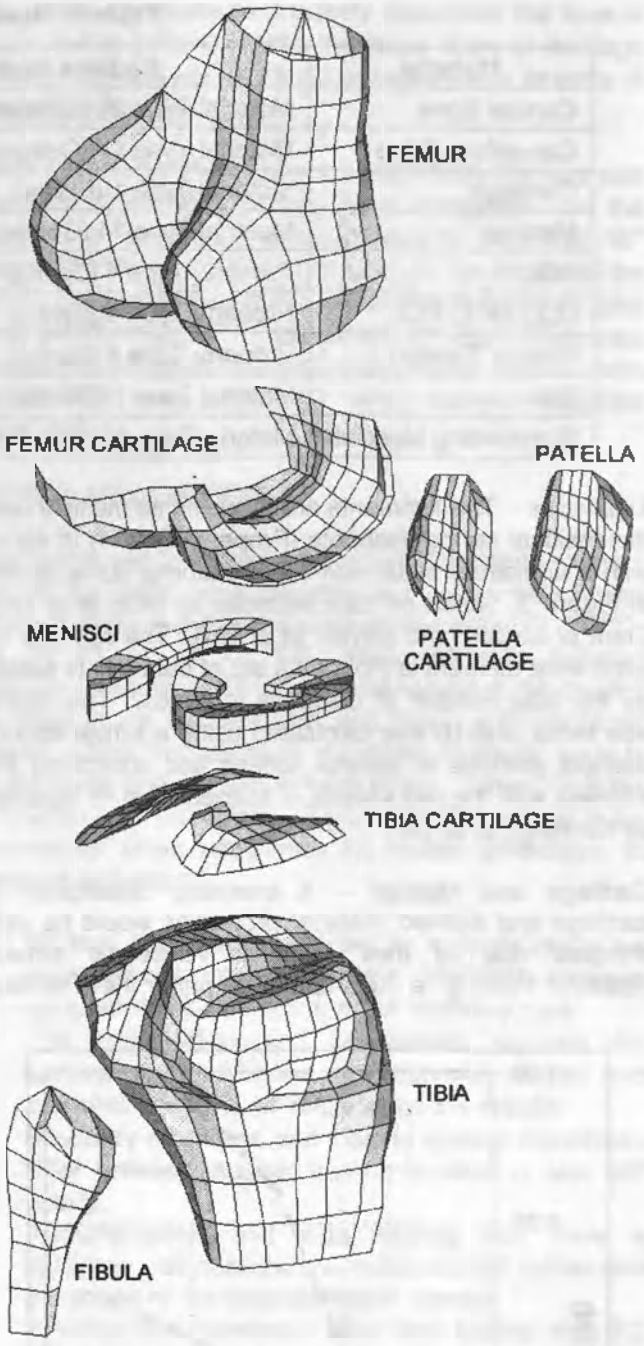

Figure 2: Knee Joint Finite Elements

While the elastic material properties for cortical and cancellous bone are reported by Viano [25] and Carter & Hayes [26], parameters describing their non-linear behavior are not available. To determine the parameters required to model the materials' non-linear behavior, a series of simulations were performed with a single shell (for cortical bone) or solid (for cancellous bone) finite element. The element was separately subjected to tension and compression along the primary (stronger) axis and the secondary (weaker) axis until element deletion. The non-linear modeling parameters were modified until the results (including strain at failure) matched the data in Cowin [27] and Evans [28] for cortical and cancellous bone, respectively. The resulting parameters are listed in Table 6. Along the primary axis, the final distortion energy failure limit for cortical bone corresponds to a maximum strain of 2.7% (-2.2%) and maximum stress of 130 MPa (-190 MPa) in pure tension (compression). The cancellous bone limit corresponds to a maximum strain of 3.3% (-4.6%) and maximum stress of 1.4 MPa (-2.1 MPa) in pure tension (compression) along the primary axis.

Table 5: Material Models and Sources

Material	Radioss Model	Property Source
Cortical Bone	Material Type 25 (Composite Shell)	Viano [25], Cowin [27]
Cancellous Bone	Material Type 14 (Composite Material)	Carter & Hayes [26], Evans [28]
Cartilage	Material Type 1 (Elastic)	Hayes, *et al.* [33]
Menisci	Material Type 14 (Composite Material)	Tissakht & Ahmed [34]
ACL	Property Type 4 (Spring)	Woo, *et al.* [29]
LCL, MCL, PCL	Property Type 4 (Spring)	Trent, *et al.* [30]
Patellar Tendon	Property Type 4 (Spring)	Noyes, *et al.* [31]
Skin	Material Type 1 (Elastic)	Ford Motor Company Hybrid III model
Surrounding Muscles	Material Type 33 (Low Density Foam)	Ford Motor Company EEVC Leg-Form model

Ligaments – The ligaments are modeled as multiple one-dimensional spring-dashpots (Property Type 4) in series with a combined static non-linear stiffness curve shown in Figure 3, based on data reported by Woo *et al.* [29], Trent *et al.* [30], and Noyes, *et al.* [31]. The stiffness for each finite element is input as a set of data points scaled by the total number of elements in series. The strain-rate factor of 0.10 was calculated using a simple spring-dashpot analysis at several speeds and comparing the stiffness with the two speeds of stiffness results reported by Kennedy, *et al.* [32].

Cartilage and Menisci – A complete description of cartilage and menisci material properties would be very complex due to their biphasic viscoelatic nature. However, during a high-speed impact, they behave elastically (Mow, *et al.* [23]). Consequently, the cartilage was modeled using Material Type 1 (Elastic), with E = 12 MPa and ν = 0.35 (Hayes, *et al.* [33]). To capture their separate matrix and collagen fiber properties, the menisci were modeled as orthotropic elastic using Material Type 14 (Composite [Solid] Material). Based on Tissakht & Ahmed [34], the menisci were given elastic moduli of 105 MPa circumferentially, 60 MPa radially, and 8 MPa out-of-plane.

Surrounding Muscles and Skin – During an impact the skin and surrounding muscles serve primarily to distribute the applied force over the irregular bone surfaces rather than absorb a significant amount of the impact energy or act as load-carrying members. In fact, around the knee joint and anterior to the tibia shaft only 5-15 mm of soft tissue is present. Because of this geometry, it is felt that the detailed compressive properties for the skin and surrounding muscles are not critical for this model.

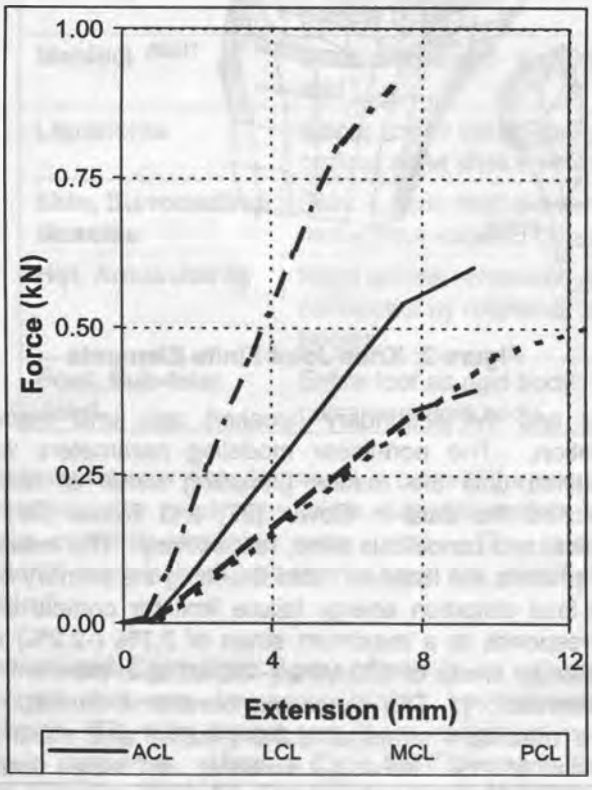

Figure 3: Ligament Stiffness Curves

Table 6: Bone Material Model Parameters

	Cortical		*Cancellous*
Parameter	***Femur***	***Others***	
ρ (kg/m^3)	1900	1900	600
E_1 (GPa)	17.0	18.0	0.3
$E_{2/3}$ (GPa)	11.0	11.0	0.07
ν	0.35	0.35	0.5
$G_{12/31}$ (GPa)	3.3	3.3	0.15
G_{23} (GPa)	3.6	3.6	0.1
b*	6.0	6.0	700
n	0.53	0.53	0.53
σ_{1yt} (MPa)	100	115	1.2
$\sigma_{2/3yt}$ (MPa)	35	40	0.5
σ_{1yc} (MPa)	145	170	1.9
$\sigma_{2/3yc}$ (MPa)	85	100	1.0

* The hardening parameter, b, has distinct definitions for Radioss Material Types 14 and 25.

As no compressive properties for lower limb muscles were available in the literature, the model uses the Confor™ foam from the EEVC Pedestrian Leg-Form for the surrounding muscles' properties. The correct bulk density of the surrounding muscles was used to achieve proper lower limb mass distribution. The skin properties come from the Hybrid III Dummy skin. When data becomes available for human skin and lower limb surrounding muscles, the model can be easily updated with these properties.

INJURY PREDICTION – As the purpose of this model is to evaluate the real-world performance of vehicle designs in lower limb injury, it is important to have an accurate method of predicting and modeling the effects of common lower limb injuries. This model is capable of predicting bone failure, ligament rupture, and meniscus tears based on local stress and strain throughout an impact. An important unique feature of this model is that the effect of hard or soft tissue injuries early in the impact event can be evaluated as the impact continues.

Bone Failure – It is critical to accurately predict bone failures since they are among the most common real-world automotive lower limb injuries [3,4,7]. In addition, the occurrence of bone failures will certainly affect the incidence or severity of secondary knee soft tissue injuries. To simulate failure, the cortical and cancellous bone material models delete elements when a distortion energy limit is exceeded. After an element is deleted, the stress in surrounding elements either increases, resulting in further element deletions and eventual loss of structural load-carrying capability (e.g. complete tibia shaft fracture), or decreases, indicating only local damage (e.g. compressive fracture of the tibial plateau).

In this failure prediction approach with an explicit solver the mesh size is not critical but the time step is important. The analysis remains stable after element deletion, due to a stabilizing algorithm applied in Radioss. While the theory supporting stabilizing algorithms remains a research topic, the technique has been used successfully in many types of crash analysis over several years.

Ligament Failure – Ligament rupture or avulsion, while less common than bone failure, is a significant cause of long-term lower limb impairment. The ability to predict the interaction between ligament ruptures and bone failures is one of the key improvements in this model. Ligament ruptures are modeled by element deletion at a specified tensile strain. Ligament avulsion is predicted by deletion of one or more cortical bone finite elements within the ligament insertion area.

Cartilage or Meniscus Tear – Although no element deletion or load drop-off is enabled for the meniscus or cartilage, the occurrence of a meniscus or cartilage injury is determined by the state of strain in the finite elements. The strain state is monitored in the output animation files. This limits the ability to precisely determine the time of injury, but is sufficient since meniscus tears or cartilage damage are unlikely to affect the incidence or severity of secondary injuries.

TIME STEP – By limiting the minimum finite element size the minimum time step has been controlled. In the whole-limb validation, the minimum time step was 10^{-4} msec. This is reasonable compared to the model of the EEVC Pedestrian Leg-Form, which has a minimum time step of 10^{-3} msec. A reasonable minimum time step allows the model to be used with vehicle models (with significantly more elements) using current computer resources.

MODEL VALIDATION

The model was validated by comparing the finite element results for static bone bending and lower limb lateral shear impacts to published cadaver test data [35, 36, 37, 38, 39, 40, 41, 42, 43, 44]. Static validation included anterior-posterior (A-P) and lateral-medial (L-M) 3-point bending of the isolated tibia and femur until structural failure. Dynamic validation consisted of lateral impacts to the lower limb simulating knee shear. Table 7 lists the validation runs performed. Several key facts need to be considered when comparing FE model predictions to physical test results:

- Physical test results reported for a single study are averaged over multiple samples. Variability between samples, while significant, is not identified here.
- The preservation and preparation methods for cadaver test specimens vary between studies and can have a significant influence on the results.
- Boundary conditions and loading speeds sometimes differ between studies, leading to more or less stiff results.
- Instrumentation and data filtering can have a significant influence on the reported peak values and the shape of the force-deflection curves.
- Physical test conditions allow less control than FE analysis. Tests may not constrain out-of-plane rotations or translations that are restricted by the FE boundary conditions. Alignment of load cells and applied forces may vary in testing, but is ensured to be exact in FE analyses.

An additional complication is that cadaver specimens come primarily from the elderly, resulting in test results that are weaker than the average for the population at large. To partially reflect the effect of age on these results, two bone material models were evaluated during the validation process. The "average properties" represents the data listed in Table 6, while the "elderly properties" were weakened to represent bone properties of a 70-90 year old male. Burstein, *et al.* [45] measured bone property reductions of approximately 8-14% for yield stress, 10-15% for ultimate stress, and 15-20% for

Table 7: Validation Runs

	Model	*Direction*	*Reference*
Static	Femur	A-P	[37,38,39,40,42]
		L-M	[40,42,43]
	Tibia	A-P	[35,36,38,40,41,42]
		L-M	[40,41,42]
Dynamic	Lower Limb	L-M Shear	[44]

ultimate strain between middle-age (40-49 years) and elderly (70-79 years) samples. To simulate these changes in the lower limb model, the bone hardening parameter (b), maximum distortion energy, and yield strengths (σ_{1yt}, $\sigma_{2/3yt}$, σ_{1yc}, $\sigma_{2/3yc}$) were reduced, as listed in Table 8, to create the "elderly properties." For the tibia, these "elderly properties" result in a prediction of bone failure at a tensile (compressive) ultimate strain of 2.2% (-1.8%) and ultimate stress of 110 MPa (-160 MPa). Note that these material properties changes alone are not intended to capture the full difference between elderly and middle-age bone properties – there are also geometrical and sectional differences, for example.

Tibia & Femur Static 3-Point Bending Validation – Cadaver test setups for 3-point bending vary in the number, age, gender, and pathology of the samples, the preservation method, the loading speed, and the boundary conditions (end treatments, load applicator size). For validation purposes, the lower limb long bone model boundary and loading conditions were designed to simulate the most common test setup. This setup consists of plaster blocks encasing 10% of the tibia and femur at the proximal and distal ends. The blocks were placed on flat plates with the bending load applied through a 25 mm diameter rod positioned at the bones' mid-shaft [42]. These conditions were simulated in the model by creating rigid bodies including nodes in the proximal and distal 10% of the bones. The distal rigid body was constrained against all translations but free to rotate while the proximal rigid body was constrained only against X (A-P) and Y (L-M) translations. A rigid body in the shape of the 25 mm diameter rod was given a fixed low-speed velocity toward the bones' mid-shaft. Initially, analyses were performed at two different velocities to verify consistent results – confirming the quasi-static intent. The bending load was measured through the interface between the rod and the cortical bone. Note that by allowing rigid body master node rotations, the model simulates a lower stiffness end condition than some of the physical tests, which may have constrained the plaster end blocks from rotating.

In all cases, bone failure consisted of a prediction of a complete transverse fracture through the same section where the bending force was applied at mid-shaft. The

Table 8: Average & Elderly Bone Material Parameters

	Tibia		*Femur*	
Property	***Average***	***Elderly***	***Average***	***Elderly***
Hardening Parameter (b)	6.0	4.0	6.0	4.0
Max. Distortion Energy	0.003	0.0021	0.003	0.0021
σ_{1yt} (MPa)	115	100	100	80
$\sigma_{2/3yt}$ (MPa)	40	35	35	30
σ_{1yc} (MPa)	170	150	150	130
$\sigma_{2/3yc}$ (MPa)	100	95	95	90

bending moment and deflection at failure were determined when the distortion energy limit was reached by an element at any location. A comparison of the force-deflection data between the present study and published cadaver test results is presented in Figure 4 (a-d), for those cadaver studies which report force-deflection data. In each of these figures, the dashed lines represent the "average properties" analysis results while the solid line represents the "elderly properties" analysis results. Cadaver test results are shown with dotted lines. A comparison of the force, bending moment, and bending deflection at bone failure for tibia and femur L-M and A-P bending is provided in Table 9. These results are discussed below.

Although the simulation predictions do not exactly match the individual reported average results, they are contained within the variation between studies. The "elderly properties" model appears to give the best prediction of the published cadaver test data. A more detailed discussion of the individual 3-point bending validation results follows below.

Femur Static 3-Point A-P Bending Validation – Several sources report 3-point bending failure properties for comparison with the FE model results produced in this study. Weber (summarized by Nyquist [40]) and Yamada [42] report similar failure properties: about 2.6 kN load, 12.3 mm deflection and 234 N-m bending moment. The test results reported by Mather [38,39] are higher, with failure at 3.2 kN load, 13.2 mm deflection, and 315 N-m bending moment. The highest average results were reported by Ehler & Losche [37], at 4.25 kN load and 12.8 mm deflection (bending moment was not reported). For comparison, the "average properties" model predicts failure at or above these test data: 4.4 kN force, 14.5 mm deflection, and 380 N-m bending moment. The "elderly properties" model failure prediction at 3.15 kN force, 11.2 mm deflection, and 270 N-m bending moment fall closest to the Mather results.

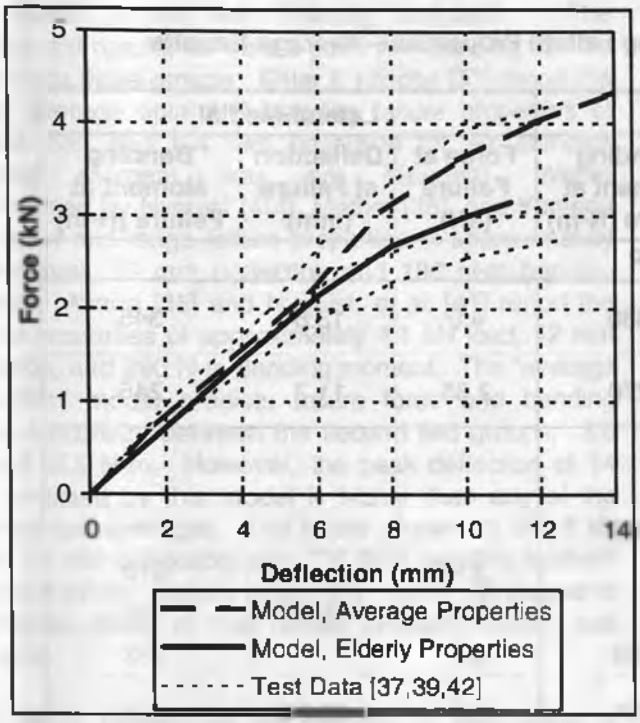

(a) Femur A-P Static 3-Point Bending

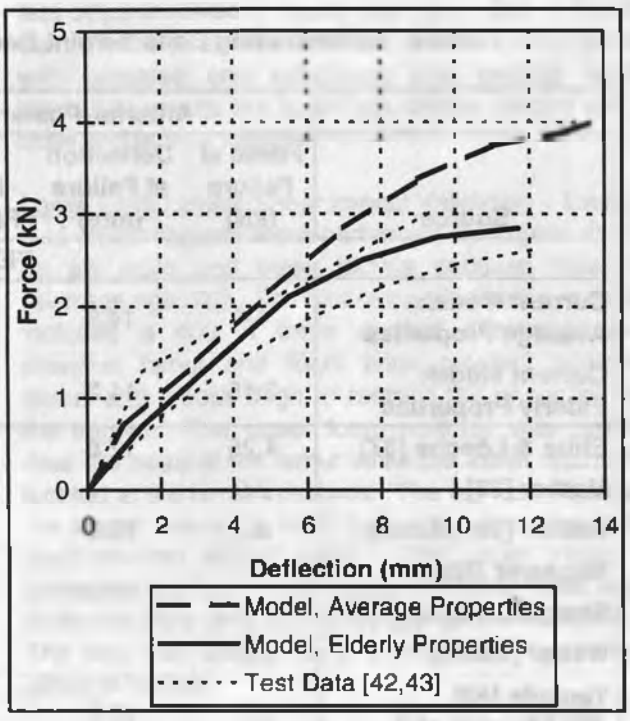

(b) Femur L-M Static 3-Point Bending

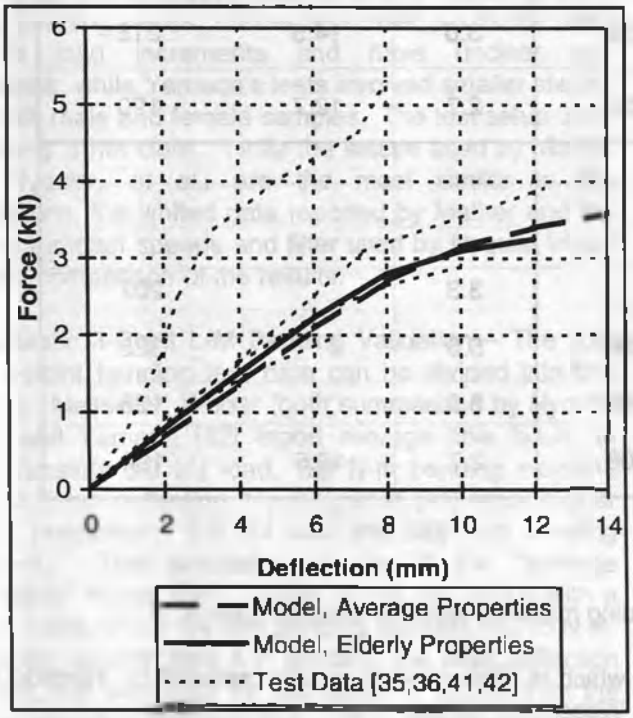

(c) Tibia A-P Static 3-Point Bending

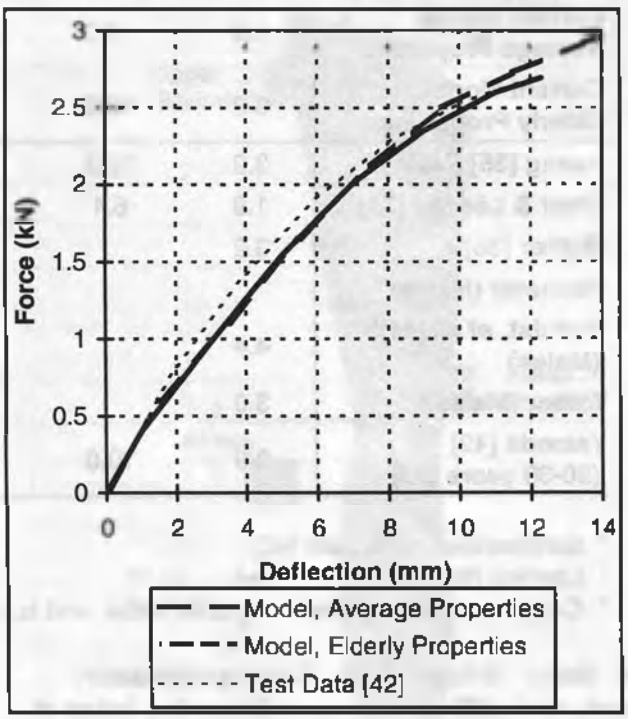

(d) Tibia L-M Static 3-Point Bending

Figure 4: Isolated Long Bone 3-Point Bending Force versus Deflection

There are several differences between these studies that can explain some of the variation in the average results. Both Weber and Ehler & Lösche applied bending loads in defined increments of 245 N and 500 N, respectively. This approach leads to under- or over-reported peak values. Also, the detailed end conditions used in each of these studies were not clearly defined, so it is not possible to say how well they match the simulation setup.

While Yamada's test setup is clear, the cadaver samples were likely of smaller stature and included both genders – leading to weaker bending properties, on average. Mather's test setup is probably the closest match to the simulation, as the cast bone ends were allowed to rotate and translate longitudinally during the test and the load was applied through a 10 mm flat plate.

Table 9: Isolated Long Bone 3-Point Bending Failure Properties – Average Results

Source	Anterior-Posterior			Lateral-Medial		
	Force at Failure (kN)	Deflection at Failure (mm)	Bending Moment at Failure (N-m)	Force at Failure (kN)	Deflection at Failure (mm)	Bending Moment at Failure (N-m)
FEMUR						
Current Model: Average Properties	4.4	14.5	380	4.0	13.6	345
Current Model: Elderly Properties	3.15	11.2	270	2.85	11.7	245
Ehler & Lösche [37]	4.25	12.8				
Mather [38]	2.9					
Mather [39] (Males)	3.2	13.2	315			
Messerer (Males)*				3.9		310
Strømsøe, *et al.* [43]				4.3	8.7	160
Weber (Males)*†	2.5		233	2.5		233
Yamada [42] (20-39 years old)	2.7	12.3	234	2.6	12.2	224
TIBIA						
Current Model: Average Properties	3.6	14.0	255	3.0	14.5	215
Current Model: Elderly Properties	3.2	12.0	230	2.7	12.7	190
Asang [35] (Males)	3.9	12.2				
Ehler & Lösche [36]	1.9	6.4				
Mather [38]	3.2					
Messerer (Males)*				3.3		207
Nyquist, *et al.* [41]‡ (Males)	4.4		290	5.0		328
Weber (Males)*†	3.0		165	3.0		165
Yamada [42] (20-39 years old)	2.9	10.0	208	2.7	12.5	194

* Summarized by Nyquist [40].
† Loading direction not reported.
‡ Complete lower leg (including tibia, fibula, and surrounding muscles) tested at several speeds.

Femur Static 3-Point L-M Bending Validation – Strømsøe, *et al.* [43] report femur L-M bending failure at 4.3 kN load, 8.7 mm deflection, and 160 N-m bending moment on average. Weber (summarized by Nyquist [40]) and Yamada [42] report failure at approximately 2.6 kN load, 12.2 mm deflection and 228 N-m bending moment. Messerer (summarized by Nyquist [40]) reports the highest failure bending moment of 310 N-m, corresponding to a force of 3.9 kN. For comparison, the "average properties" model predicts failure at or above the reported test averages: 4.0 kN force, 13.6 mm deflection, and 345 N-m bending moment. The "elderly properties" model predicts bone failure at 2.85 kN force, 11.7 mm deflection, and 245 N-m bending moment, which is similar to the results reported by Yamada and Weber.

Again, there are differences between the studies that can explain some of this variation. Both Strømsøe, *et al.*, and Messerer performed 3-point bending with two fixed rods and one moving rod – resulting in a shorter test span than the other studies. As mentioned above, Weber applied bending loads in 245 N defined increments with unclear end conditions, while Yamada's results are based on shorter stature and mixed gender samples.

Tibia Static 3-Point A-P Bending Validation – The physical test results for tibia 3-point A-P bending can be divided into three groups. Ehler & Lösche [37] report the lowest average tibia A-P bending failure properties of 1.9 kN load and 6.4 mm deflection for six samples (bending moment was not reported). Weber (summarized by Nyquist [40]), Mather [38], and Yamada [42] report mid-range failure properties of approximately 3.0 kN load, 10 mm deflection and 180 N-m bending moment. Asang [35] and Nyquist, *et al.* [41] report the highest properties of approximately 4.1 kN load, 12 mm deflection, and 290 N-m bending moment. The "average properties" model predicts failure force and bending moment mid-way between the second two groups: 3.6 kN and 255 N-m. However, the peak deflection of 14 mm predicted by this model is higher than any of the reported test averages. The failure properties of 3.2 kN force, 12 mm deflection, and 230 N-m bending moment predicted by the "elderly properties" model fall closest to the middle group of test results (Weber, Mather, and Yamada).

Test setup differences are present in this group of studies as well. Nyquist performed bending impacts at various speeds and used a low (100 Hz) filter. As in the femur bending cases, Weber and Ehler & Lösche used defined load increments and have unclear end conditions, while Yamada's tests involved smaller stature and both male and female samples. The test setup used by Asang is not clear. While the setups used by Mather and Nyquist, *et al.*, are the most similar to the simulations, the limited data reported by Mather and the different impact speeds and filter used by Nyquist inhibit a direct comparison of the results.

Tibia Static 3-Point L-M Bending Validation – The tibia L-M 3-point bending test data can be divided into two groups. Messerer, Weber (both summarized by Nyquist [40]), and Yamada [42] report average tibia failure at approximately 3.0 kN load, 190 N-m bending moment, and 12.5 mm deflection. Nyquist, *et al.* [41] report higher failure properties: 5.0 kN load and 328 N-m bending moment. The simulation results of the "average properties" model were closest to the first group with a failure force of 3.0 kN and bending moment of 215 N-m. However, as with tibia A-P bending, the peak deflection of 14.5 mm predicted by this model is higher than the single reported test average. The "elderly properties" model's predicted failure force of 2.7 kN and bending moment of 190 N-m were also similar to the first group of results, while its predicted peak deflection of 12.7 mm was close to the average reported by Yamada.

The variation between the tibia L-M bending results can be understood by looking at the test setups. Like the tibia A-P tests, the Nyquist, *et al.*, results are based on various impact speeds and a 100 Hz filter. Messerer's test setup involved a shorter test span (2/3 of the bone) than the other studies. Weber used incremental loads with unstated end conditions and loading direction. Yamada's results are based on shorter stature and both male and female samples.

Lower Limb Lateral Shear Impact Validation – Lower limb L-M shear impacts were performed by Kajzer *et al.* [44] on six male and three female cadaver lower limbs (average age: 78). The test setup, illustrated in Figure 5, included a 400 N force applied downward on the proximal femur and foam pads pressed against the lateral and medial thigh to restrain the upper leg during the impact. The upper foam restraint was positioned near the head of the femur while the lower restraint was located at the femur condyles. The leg was impacted on the lateral side at 15 km/h by a 40 kg impactor with two foam-covered impact faces. The upper impact face contacted the leg 40 mm below the lower foam restraint while the lower face contacted just above the ankle joint. The foot was placed on a mobile plate to reduce the effect of friction.

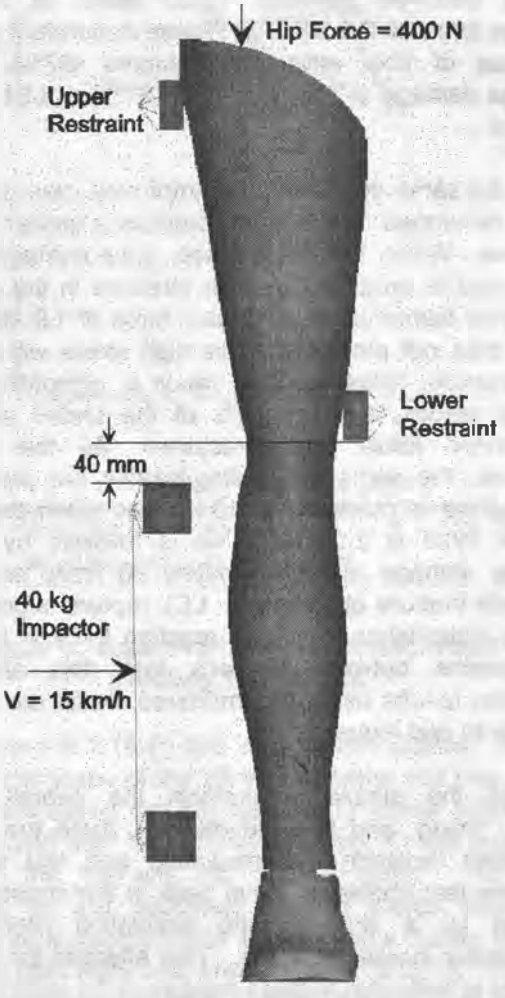

Figure 5: Lower Limb Lateral Shear Impact Setup (Front View)

To simulate the test condition, solid finite elements modeling the foam restraints were located at the lateral upper thigh and medial lower thigh in contact with the skin. These foam blocks were constrained against all translations. A concentrated load of 400 N was applied vertically downward at the proximal femur rigid body. Solid elements modeling the impactor foam blocks were attached to a 40 kg rigid body and positioned just above the ankle and just below the knee joint. The rigid body master node was constrained in X (A-P) and Z (superior-inferior) translations and given an initial velocity of 15 km/h toward the leg in the medial direction. The foot rigid body master node was constrained in vertical translation and all rotations. The impactor faces were located 42 mm away from the leg to allow 10 msec for the vertical pre-load to compress the knee joint.

Using high-speed film, Kajzer estimated that the first injuries occurred during the initial knee impact force peak (1.7-2.5 kN) after approximately 5 msec. For the male specimens, these initial contact injuries consisted of fibula head fractures (50%)*. As the impact proceeded, a second injury type occurred, due to the transfer of load through the knee joint. Kajzer estimated that these injuries occurred between 15-20 msec, at a knee reaction force of 2.2-3.0 kN. These secondary injuries consisted of tibia eminence fractures (67%), femur cartilage damage (67%), and ACL (67%) or LCL (50%) ruptures.

Under the same conditions, the improved lower limb FE model developed in this study predicts a similar impact response. Within the first 8 msec, bone damage in the fibula head is predicted by high stresses in the cortical bone finite elements, at an impact force of 1.9 kN. The model does not predict that this high stress will lead to bone fracture, however. This result is compatible with Kajzer's results, as only 50% of the tested samples experienced fibula head fracture. As the impact continues, the same knee joint injuries are predicted. ACL rupture is predicted at 13.5 msec when the knee reaction force is 2.0 kN. This is followed by femur cartilage damage at approximately 20 msec and tibia eminence fracture at 25 msec. LCL rupture is predicted at 25.6 msec when the knee reaction force is 2.6 kN. Comparisons between Kajzer's test data and the simulation results using the improved model are shown in Table 10 and Figure 6.

Although the simulation predicts the overall injury pattern, timing, and force levels well, there are a few differences between the simulation and test results. While the test shows an initial peak in the impact force followed by a drop-off, the simulation predicts a continuously increasing force. This effect in the Kajzer test data is likely due to fibula fracture in the reported test sample. In the simulation, however, the fibula does not fracture, so the impact force does not decrease. The lack of fibula fracture in the simulation also is likely the reason that the predicted impact force over time is higher than the test results.

Table 10: Lower Limb L-M Shear Impact Results (Male Specimens)

		Kajzer, et al. [44]	*Present Study*
Contact Injury	**Type**	Fibula head fractures (50% of samples).	Local bone damage in fibula head (no fracture).
	Time	5 msec	8 msec
	Force	1.7 – 2.5 kN	1.9 kN
Knee Joint Injury	**Type**	Tibia eminence fracture, femur cartilage damage, and ACL & LCL rupture	Tibia eminence fracture, femur cartilage damage, and ACL & LCL ruptures
	Time	15 – 20 msec	13.5 – 25.4 msec
	Reaction Force	2.2 – 3.0 kN	2.0 – 2.6 kN

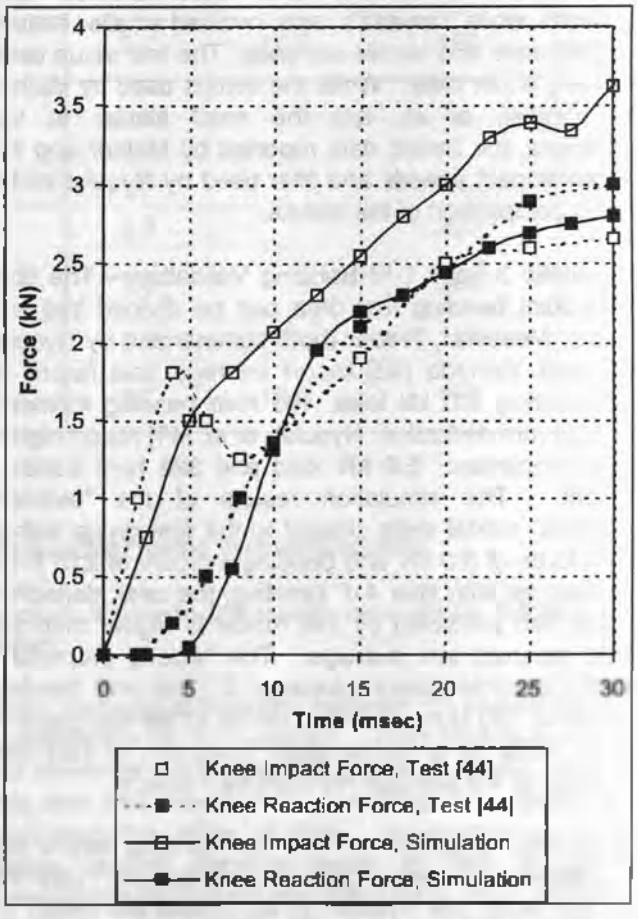

Figure 6: Knee Impact and Reaction Forces During Lateral Shear Impact

* Percentages in parentheses represent the proportion of male specimens in which this injury was observed.

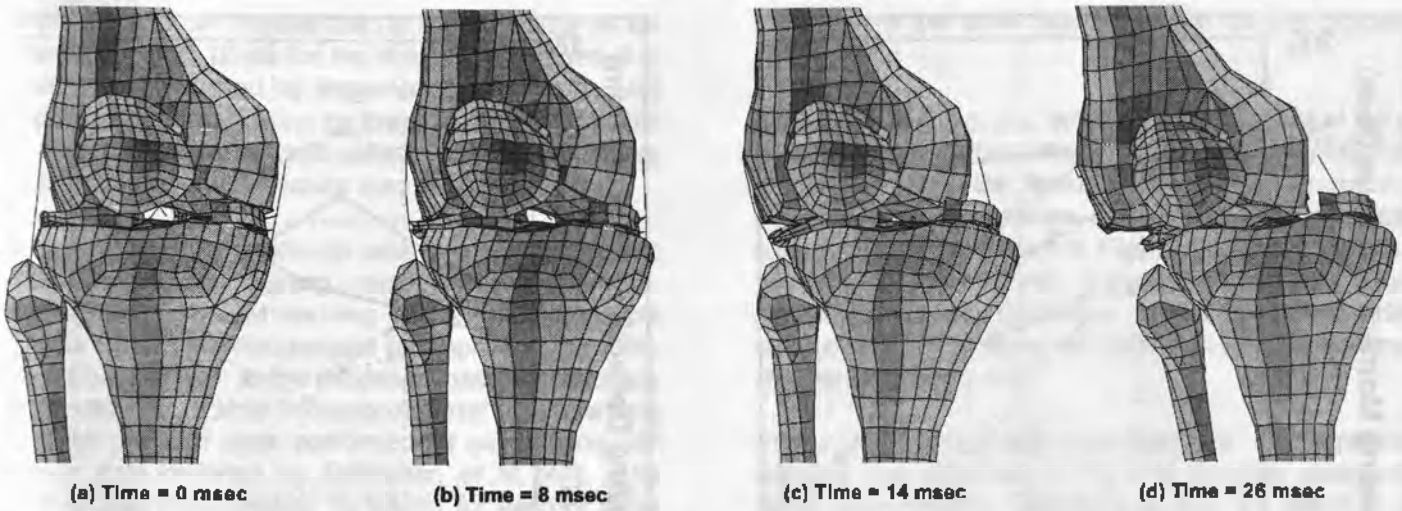

Figure 7: Lower Limb L-M Shear Impact – Knee Joint Deformation

Two benefits of the improved model are illustrated by these results. First, by independently predicting different types of damage, the model can predict the sequence of injuries. In this case, the model predicts that the ACL will rupture before the LCL despite the lack of torsion in the setup. A second benefit of the model is that the kinematics and deformation throughout the impact can be studied for greater understanding. This process was used to determine that since the upper shear impactor face contacts 6 msec before the lower face, the tibia initially rotates about the ankle joint. This rotation minimizes the LCL strain while increasing the ACL strain, resulting in the prediction of ACL rupture before LCL rupture. Figure 7 illustrates the knee joint deformation at the times of injury.

COMBINED LOADING CONDITIONS

Under real-world conditions the lower limb is subjected to a combination of axial load, shear loads, and bending moments. In particular, lower limb bending injuries resulting from sporting or pedestrian impacts typically involve an initial vertical load (body mass) in addition to an impact bending moment. To predict the susceptibility of the lower limb bones to failure under these real-world conditions, it is important to understand how the bending stiffness and strength of the bones change when subjected to an axial pre-load. Since this condition is difficult to simulate in physical testing, most cadaver lower limb bending tests are performed with no applied axial load. The validated model with the bone "elderly properties" was used to investigate the influence of an axial pre-load on isolated tibia and femur bending.

Simulations of tibia and femur bending with zero axial pre-load were performed as part of the model validation. The same models were used to evaluate bending with non-zero pre-load. As in the validation runs, the proximal and distal 10% of the bones were included in separate rigid bodies, with the distal rigid body constrained in all translations and the proximal rigid body constrained only

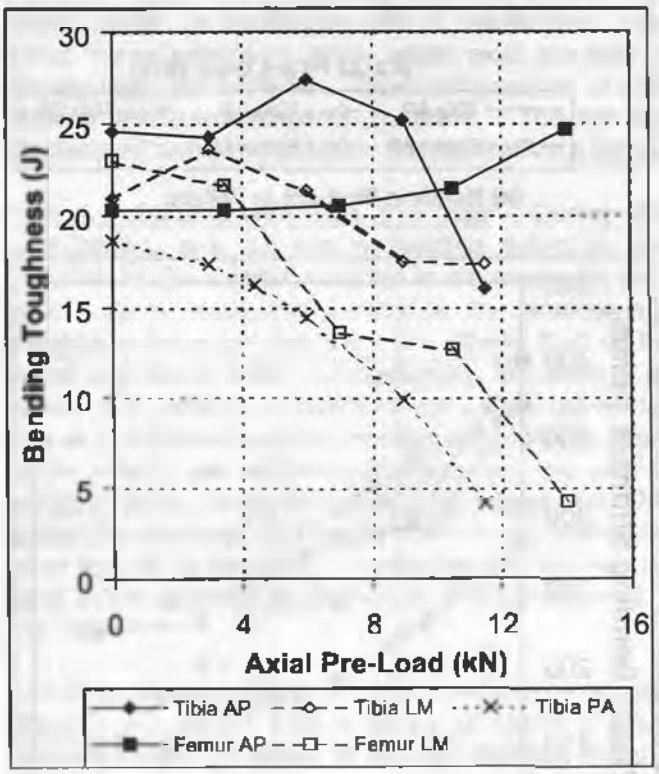

Figure 8: Axial Pre-Load Effect on 3-Point Bending Toughness

with respect to X (A-P) and Y (L-M) translations. A rigid body in the shape of the 25 mm diameter rod was given a fixed low-speed velocity toward the bones' mid-shaft. The bending load was measured through the interface between the rod and the cortical bone. The only changes for the combined loading cases were the addition of a concentrated vertical force acting on the proximal rigid body and greater initial distance between the impactor and the bone to allow the pre-load to take effect. Due to the femur and tibia geometry, an axial load applied at the proximal end through the center of the hip or knee joint will result in eccentricity throughout the

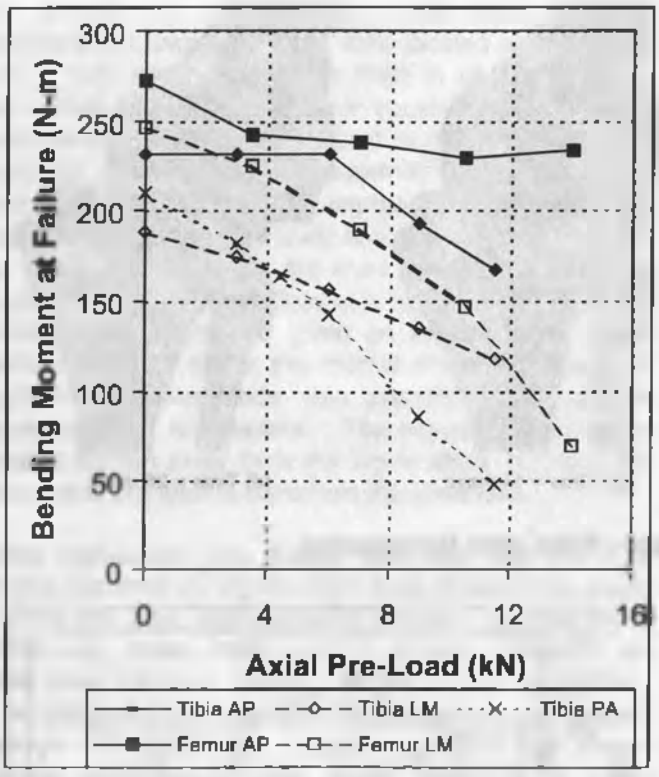

(a) Bending Moment at Failure

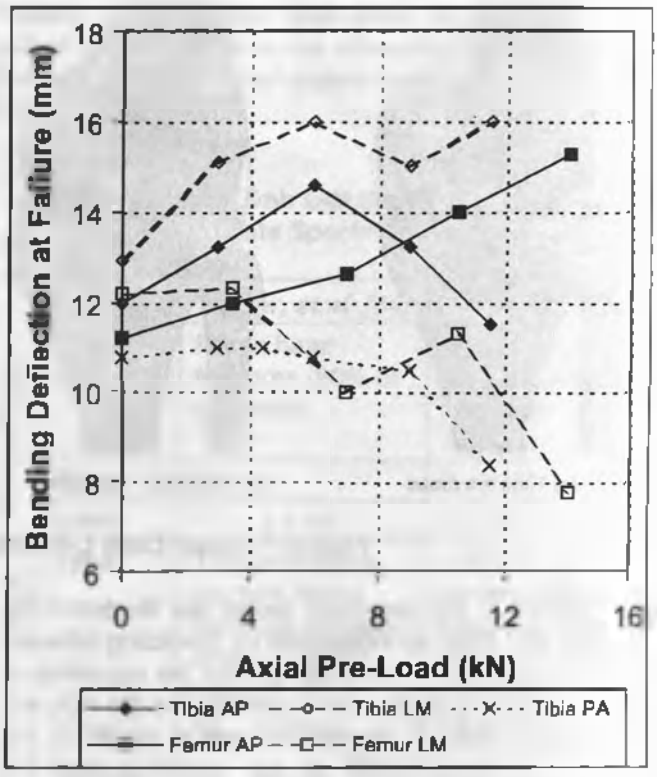

(b) Bending Deflection at Failure

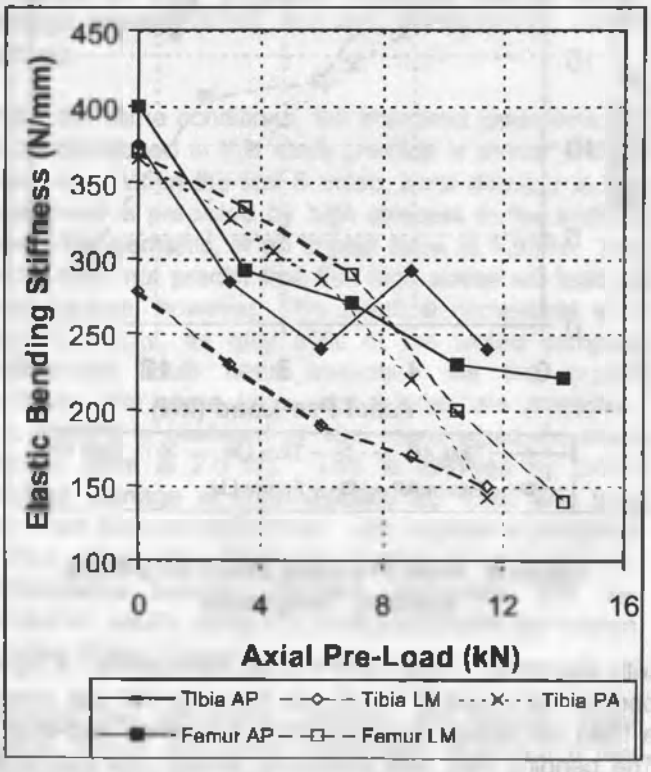

(c) Elastic Bending Stiffness

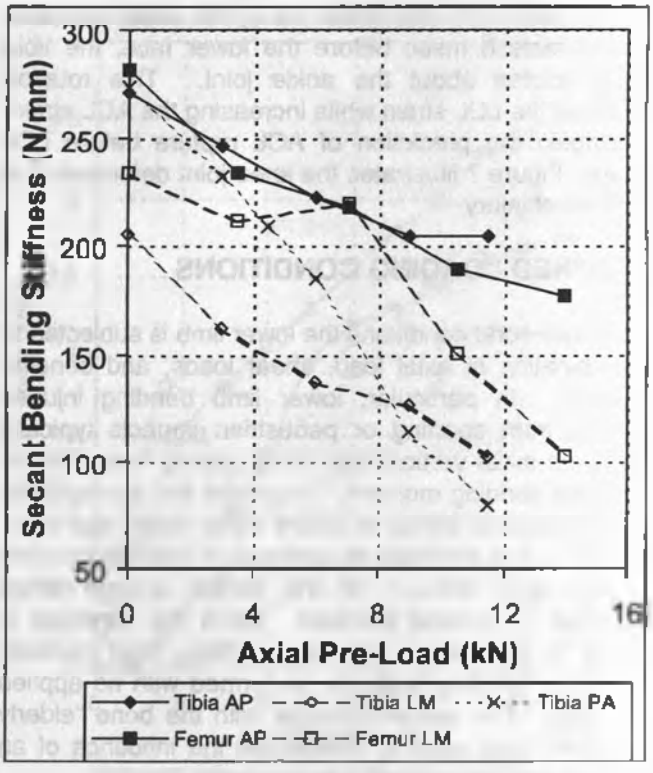

(d) Secant Bending Stiffness

Figure 9: Axial Pre-Load Effect on 3-Point Bending Properties

shaft. Thus, in these simulations—as in the real world—the bones are subjected to an eccentric axial load, a shear force, and a bending moment.

A separate analysis was performed to determine the maximum axial load the bones could withstand before shaft failure. The rigid bodies simulating plaster end casts allowed no failures at the proximal & distal ends.

This predicted shaft fracture load is approximately 14 kN for the femur and 12 kN for the tibia. The tibia result is similar to that reported by Begeman & Paravasthu [46] for static axial compression on lower legs (including tibia and fibula) with plaster end casts. Over five samples they found an average fracture load of 10.9±2.5 kN.

After predicting the maximum axial compressive loads, sixteen combined loading cases were simulated, including A-P and L-M bending of the femur and tibia with four levels of axial pre-load (at approximately 25%, 50%, 75%, and 95% of the maximum loads). In addition, five simulations of tibia Posterior-Anterior (P-A) bending with axial pre-load were performed for comparison with cadaver data reported by Schrieber, *et al.* [47]. The bending toughness (energy to failure) for each of these cases is plotted in Figure 8, while the elastic and secant bending stiffness, the deflection at failure, and the bending moment at failure are shown in Figure 9. Each data point corresponds to a single simulation result. Note that the reported bending moment at failure is only due to the applied 3-point bending force, and does not include the bending moment induced by the axial load eccentricity.

Figure 9 shows that the bending moment at failure decreases with increasing axial load – this is more pronounced in the L-M direction for both bones. These results indicate a greater risk of bone failure under an applied axial load. Since the lower limb axial load increases with activity level (i.e. standing, walking, or running), it appears that the susceptibility to failure will increase as well. Unfortunately, it is at higher activity levels that bending loads due to tripping or impact also become more pronounced.

Not shown in the figures are the predicted strains and deformations within the bones during these simulations. Since predicting the stress, strain, and deformation throughout the bone is one of the benefits of a numerical simulation, some discussion of these results is warranted.

Femur A-P Bending with Axial Pre-Load – Under an applied axial pre-load, the femur deflects up to 8.4 mm in the anterior direction at mid-shaft. This is due to a negative bending moment resulting from the negative eccentricity from the femur geometry. The negative moment counteracts the positive moment during 3-point bending. The magnitude of the eccentricity increases with the axial pre-load. This negative bending moment results in a compressive strain of -1.2% on the posterior side and a tensile strain of +0.5% on the anterior side at mid-shaft. During A-P bending, the applied moment acts first to re-balance the strain distribution by decreasing the tensile strain on the anterior side and the compressive strain on the posterior side. Then the bending moment increases the compressive strain on the anterior side until bone failure in compression. This is in contrast with A-P bending failure under zero axial force where the bone fails in tension on the posterior side.

Under A-P bending, the femur bending moment at failure is relatively insensitive to axial pre-loading The maximum bending moment the femur can withstand in the A-P direction does not change significantly with increasing axial pre-load, as shown in Figure 9. Also during A-P bending, the femur first straightens and then bends posteriorly. This effectively increases the bending deflection at failure since the deflection is measured from the first point of contact.

Femur L-M Bending with Axial Pre-Load – No significant bending was observed in the L-M direction during the femur axial loading. Because of this, the effect of an applied L-M bending moment on an axially pre-loaded femur is to increase the existing compressive stress on the lateral part of the posterior side and the existing tensile stress on the medial part of the anterior side. Since the compressive strain under axial pre-load is already high, the bone fails under compression at mid-shaft in the lateral/posterior quadrant. The bending moment and deflection at failure are reduced as a result.

Tibia A-P Bending with Axial Pre-Load – During tibia axial loading, only 3.0 mm of bending deflection was observed in the anterior direction at the maximum axial force. As a result, the strains on the anterior and posterior sides of the tibia are much smaller than on the lateral and medial sides. Consequently, the effect of an applied A-P bending moment on an axially pre-loaded tibia is to increase both the existing compressive stress in the anterior part of the medial side and the existing tensile stress in the posterior part of the lateral side. Due to the tibia geometry, the tensile strain concentrates in a small area of the section, resulting in tensile failure of the bone in the posterior medial corner in the distal third of the tibia.

In A-P bending the tibia is initially unaffected by an axial pre-load, but as the load is increased above 6 kN, it begins to show an effect in reduced bending moment and deflection at fracture.

Tibia L-M Bending with Axial Pre-Load – Under an applied axial pre-load, the tibia deflects up to 7.5 mm in the lateral direction at mid-shaft. This bending imparts a compressive strain of -1.2% on the posterior side and a tensile strain of +0.4% on the lateral side in the distal third of the shaft. During L-M bending, the applied moment first re-balances the strain distribution by decreasing the tensile strain on the lateral side and the compressive strain on the medial side. As the bending moment continues to increase, the compressive strain on the lateral side increases until bone failure in compression. This is in contrast with L-M bending failure under zero axial load where the bone fails in tension on the medial side. In terms of deformation, the femur first straightens and then bends medially. This effectively

increases the bending deflection at failure since the deflection is measured from the first point of contact.

Tibia P-A Bending with Axial Pre-Load – As mentioned above, the tibia undergoes up to 3.0 mm of bending deflection in the anterior direction at the maximum axial force. An applied Posterior-Anterior bending force increases the existing anterior tensile stress and posterior compressive stress. This results in a much more pronounced reduction of strength in P-A bending versus A-P bending. Both with and without applied axial loads, tibias subjected to P-A bending failed in tension on the anterior face at mid-shaft.

Schreiber, *et al.* [47] report on intact lower legs (including tibia and fibula) subjected to P-A bending. It is useful to compare the model predictions with this test data, although an isolated tibia will be weaker than an intact lower leg. In quasi-static 3-point P-A bending, Schreiber found an average mid-shaft bending moment at fracture of 241±49 N-m. The isolated tibia simulated here was capable of resisting a P-A bending moment of 210 N-m. In dynamic P-A bending, Schreiber reports a 19% decrease in the bending moment at fracture due to the application of a 4.448 kN load. Under this axial load, the current model predicts a similar 22% reduction in P-A bending moment at fracture.

DISCUSSION

Model Limitations – One of the limitations of this model is that it represents an average for a particular segment of the population (50th percentile male). Other segments (e.g., 5th percentile females, children, elderly) may have different responses to an impact. This model cannot with certainty determine the effects of design changes on these other segments of the population, although some attempt has been made to capture the elderly properties at least for bone failure risk. It will be possible to change the material parameters without changing the geometry to determine the loading conditions at which injury occurs for other segments of the population. Another limitation of having a model representing an average is that even within the target population segment significant variation exists between individuals. Results from this model cannot be applied universally even within this population segment.

Because the model strikes a balance between number of elements and precision of geometry, detailed stresses and strains may not be directly comparable to test results. The macro behavior of the model was most important, and has been confirmed. An example of this limitation is the modeling of the cartilage as a single layer of elements – only the compressive properties are captured. Another example is the single set of spring-dashpot elements for the ligaments rather than a separate set for each fiber bundle. For the macro behavior, the fiber bundles are not critical, but because of this limitation, the model cannot provide information on the strain in individual fiber bundles.

Furthermore, the model does not fully describe the ankle and hip joints. While this limitation is not critical with respect to pedestrian impacts, it is more important for vehicle occupant injury assessment. A parallel project developing the detailed ankle joint properties will enable a more complete lower limb model in the future.

Tibia Index – The combined loading conditions investigated as a model application are closely related to the Tibia Index, defined by:

$$\frac{F}{F_{cr}}+\frac{M}{M_{cr}}\le 1, \qquad (1)$$

where F_{cr} = 35.9 kN and M_{cr} = 225 N-m for a 50th percentile male. This equation predicts that as the axial load (F) increases, the bending moment (M) must decrease to prevent bone failure. In terms of the combined loading conditions application, this indicates that the bending moment at fracture will decrease with increasing axial pre-load. Figure 9(a) shows this trend for both A-P and L-M bending. This opens up a new avenue for using the improved lower limb model to investigate the efficacy of the Tibia Index in predicting tibia failure.

Future Research – There are several areas of further work that will enhance the capability and usefulness of this model:

- Further validate the model under different impact conditions, particularly those to which a seated occupant is subject.
- Identify the buckling and bending properties of the whole limb under axial loading.
- Merge with existing ankle/foot models to increase the ability to predict vehicle occupant injuries.
- Modify the properties to represent 95th percentile male, 5th percentile female, and 6-year-old child lower limbs.
- Modify the physiology to represent different levels of knee flexion.
- Model the ligaments as multiple fiber bundles.
- Investigate the lower limb impact response under different loading conditions.

This study has also identified some areas where additional physical testing is needed:

- Static and dynamic non-linear stress-strain curves for cortical and cancellous bone
- Tensile load-deflection (including rupture) properties for the ligaments under various strain rates
- Non-linear compressive properties of surrounding muscles, menisci, and cartilage

- Tensile properties of skin
- Whole limb static bending and torsion properties, beyond the elastic range

The simulation of a vehicle-pedestrian impact is a straightforward application of this model. Simulation of a vehicle occupant's lower limb would require the physiology changes mentioned above for leg flexion, and would benefit from additional validation.

CONCLUSIONS

An improved lower limb model has been developed and validated against long bone static 3-point bending and dynamic shear impact of cadaver whole lower limbs. This model can be used in pedestrian impact analysis to better understand the detailed biomechanical results of proposed vehicle design changes. It can also have application in the investigation or development of derived injury criteria. The model includes enough detail to capture the common injuries of the thigh, knee, and leg, while maintaining a reasonable element size to avoid time step issues. The model has been used to study the effects of biological pre-loads on the bending properties of the long bones.

ACKNOWLEDGMENTS

The authors would like to thank Paul Bedewi for providing the scanned bone IGES surfaces.

REFERENCES

1. *Traffic Safety Facts 1998*, U.S. Department of Transportation, National Highway Traffic Safety Administration, 2000.
2. Morgan R, Eppinger R, Hennessey BC, "Ankle Joint Injury Mechanism for Adults in Frontal Automotive Impact." *Proc. 35th Stapp Car Crash Conference*, Paper # 912902, 1991.
3. Wykowski E, Sinnhuber R, Appel H, "Finite Element Model of Human Lower Extremities in a Frontal Impact." *Proc. IRCOBI International Conference on the Biomechanics of Impacts*, pp. 101-116, 1998.
4. Huelke DF, Compton TW, Compton CP, "Lower Extremity Injuries in Frontal Crashes: Injuries, Locations, AIS and Contacts." The Society of Automotive Engineers Paper # 910811, 1991.
5. Isenberg RA, Walz M, Chidester C, Kaufman R, "Pedestrian Crash Data Study—an Interim Evaluation." *Proc. 15th International Technical Conference on Enhanced Safety of Vehicles*, pp. 1396-1407, 1996.
6. Sakurai M, Kobayashi K, Ono K, Sasaki A, "Evaluation of Pedestrian Protection Test Procedure in Japan – Influence of Upper Body Mass on Leg Impact Test." *Proc. 14th International Technical Conference on Enhanced Safety of Vehicles*, Paper # 94-S7-O-01, pp. 1114-1130, 1994.
7. Ashton SJ and Mackay GM, "Some Characteristics of the Population Who Suffer Trauma as Pedestrians When Hit by Cars and Some Resulting Implications." *Proc. IRCOBI International Conference on the Biomechanics of Impacts*, pp. 39-48, 1979.
8. Bedewi PG, *The Biomechanics of Human Lower Extremity Injury in the Automotive Crash Environment.* Doctoral Dissertation: George Washington University, 1998.
9. Bermond F, Ramet M, Bouquet R, Cesari D, "A Finite Element Model of the Pedestrian Leg in Lateral Impact." *Proc. 14th International Technical Conference on Enhanced Safety of Vehicles*, Paper # 94-S1-O-15, pp. 199-209, 1994.
10. Yang JK, Wittek A, Kajzer J, "Finite Element Model of the Human Lower Extremity Skeleton System in Lateral Impact." *Proc. IRCOBI International Conference on the Biomechanics of Impacts*, pp. 377-388, 1996.
11. Bendjaballah MZ, Shirazi-Adl A, Zukor DJ, "Finite Element Analysis of Human Knee Joint in Varus-Valgus." *Clinical Biomechanics* **12**(3): 139-148, 1997.
12. Li G, Gil J, Kanamori A, Woo SLY, "A Validated Three-Dimensional Computational Model of a Human Knee Joint." *Journal of Biomechanical Engineering* **121**: 657-662, 1999.
13. Iwamoto M, Tamura A, Furusu K, Kato C, Miki K, Hasegawa J, Yang, KH, "Development of a Finite Element Model of the Human Lower Extremity for Analyses of Automotive Crash Injuries." Society of Automotive Engineers, Paper # 2000-01-0621, 2000.
14. Cristofolini L, Viceconti M, Cappello A, Toni A, "Mechanical Validation of Whole Bone Composite Femur Models." *Journal of Biomechanics* **29**(4): 525-535, 1996.
15. Cristofolini L, Viceconti M, "Mechanical Validation of Whole Bone Composite Tibia Models." *Journal of Biomechanics* **33**: 279-288, 2000.
16. "The National Library of Medicine's Visible Human Project," http://www.nlm.nih.gov/research/visible/visible_human.html.
17. Warwick R and Williams PL, ed., *Gray's Anatomy: 35th British Edition*, pp. 360-369. Philadelphia: W.B. Saunders Co., 1973.
18. Yang JK and Kajzer J, "Computer simulation of impact response of the human knee joint in car-pedestrian accidents." *Proc. 36th Stapp Car Crash Conference*, Paper # 922525, pp. 203-217, 1992.
19. Moeinzadeh MH and Engin AE, "Dynamic Modeling of the Human Knee Joint." *Computational Methods in Bioengineering, Proc. 1988 WAM*, BED **9**: 145-156. The American Society of Mechanical Engineers, 1988.
20. Girgis FG, Marshall JL, Al Monajem ARS, "The Cruciate Ligaments of the Knee Joint: Anatomical, Functional, and Experimental Analysis." *Clinical Orthopaedics and Related Research* **106**: 216-31, 1975.

21. Mow VC and Hayes WC, ed., *Basic Orthopaedic Biomechanics*, pp. 267-278. Philadelphia: Lippincott-Raven, 1997.
22. Mow VC, Ratcliffe A, Woo SL, ed., *Biomechanics of Diarthroidal Joints*, pp. 202 & 261. New York: Springer-Verlag, 1990.
23. Mow VC, Arnoczky SP, Jackson DW, ed., *Knee Meniscus: Basic and Clinical Foundations*, Pp. 54 & 94, .New York: Raven Press, 1992.
24. Keyak JH and Rossi SA, "Prediction of Femoral Fracture Load Using Finite Element Models: An Examination of Stress- and Strain-Based Failure Theories." *Journal of Biomechanics* **33**(2): 209-214, 2000.
25. Viano DC, "Biomechanics of Bone and Tissue: A Review of Material Properties and Failure Characteristics." The Society of Automotive Engineers Paper # 861923, 1986.
26. Carter DR and Hayes WC, "The Compressive Behavior of Bone as a Two-Phase Porous Structure." *Journal of Bone and Joint Surgery* **59A**(7): 954-961, 1977.
27. Cowin SC, *Bone Mechanics*, p. 117. Boca Raton: CRC Press, 1989.
28. Evans FG, *Biomechanical Studies of the Musculo-Skeletal System*, p. 57. Springfield, IL: C.C. Thomas, 1961.
29. Woo SLY, Hollis M, Adams DJ, Lyon RM, Takai S, "Tensile Properties of the Human Femur – Anterior Cruciate Ligament – Tibia Complex: The Effects of Specimen Age and Orientation." *The American Journal of Sports Medicine* **19**(3): 217-225, 1991.
30. Trent PS, Walker PS, Wolf B, "Ligament Length Patterns, Strength, and Rotational Axes of the Knee Joint." *Clinical Orthopaedics and Related Research* **117**: 263-70, 1976.
31. Noyes FR, Butler DL, Grood ES, Zernicke RF, Hefzy MS, "Biomechanical Analysis of Human Ligament Grafts used in Knee-Ligament Repairs and Reconstructions." *Journal of Bone and Joint Surgery* **66A**(3): 344-352, 1984.
32. Kennedy JC, Hawkins RJ, Willis RB, Danylchuk KD, "Tension Studies of Human Knee Ligaments." *Journal of Bone and Joint Surgery* **58A**: 350-355, 1976.
33. Hayes WC, Swenson LW Jr., Schurman DJ, "Axisymmetric Finite Element Analysis of the Lateral Tibial Plateau." *Journal of Biomechanics* **11**: 21-33, 1978.
34. Tissakht M and Ahmed AM, "Determination of the Static Tensile Stress-Strain Characteristics of the Human Menisci and Derivation of the Matrix and Fibre Properties." *Advances in Bioengineering*, BED **26**: 107-110, The American Society of Mechanical Engineers, 1993.
35. Asang E, "Experimental Biomechanics of the Human Leg: A Basis for Interpreting Typical Skiing Injury Mechanisms." *Orthopedic Clinics of North America* **7**(1): 63-73, 1976.
36. Ehler VE and Lösche H, "Die Menschliche Tibia Unter Biegebelastung." *Beitr. Orthop.* **17**(5): 291-304, 1970.
37. Ehler VE and Lösche H, "Biegeversuche am Menschlichen Femur." *Beitr. Orthop.* **17**(5): 304-314, 1970.
38. Mather BS, "Correlations Between Strength and Other Properties of Long Bones." *Journal of Trauma* **7**(5): 633-638, 1967.
39. Mather BS, "Variation with Age and Sex in Strength of the Femur." *Medical and Biological Engineering* **6**: 129-132, 1968.
40. Nyquist GW, "Injury Tolerance Characteristics of the Adult Human Lower Extremities Under Static and Dynamic Loading." The Society of Automotive Engineers Paper # 861925, 1986.
41. Nyquist GW, Cheng R, El-Bohy AAR, King AI, "Tibia Bending: Strength and Response." The Society of Automotive Engineers Paper # 851728, 1985.
42. Yamada H, *Strength of Biological Materials*, pp. 59-62. Evans FG, Editor. Baltimore: Williams & Wilkins, 1970.
43. Strømsøe K, Høiseth A, Alho A, Kok WL, "Bending Strength of the Femur in Relation to Non-Invasive Bone Mineral Assessment." *Journal of Biomechanics* **28**(7): 857-867, 1995.
44. Kajzer J, Cavallero C, Ghanouchi S, Bonnoit J, Ghorbel A, "Response of the Knee Joint in Lateral Impact: Effect of Shearing Loads." *Proc. IRCOBI International Conference on the Biomechanics of Impacts*, pp. 293-304, 1990.
45. Burstein AH, Reilly DT, Martens M, "Aging of Bone Tissue: Mechanical Properties." *Journal of Bone and Joint Surgery* **58A**: 82-86, 1976.
46. Begeman P and Paravasthu N, "Static and Dynamic Compression Loading of the Lower Leg." *Proc. 7th Injury Prevention Through Biomechanics Symposium*, 1997.
47. Schreiber P, Crandall J, Micek T, Hurwitz S, Nusholtz GS, "Static and Dynamic Bending Strength of the Leg." *Proc. IRCOBI International Conference on the Biomechanics of Impacts*, pp. 99-113, 1997.